Lightweight UAV Digital Elevation Models and Orthoimagery for environmental applications: data accuracy evaluation and potential for river flood risk modelling.

Corresponding Author: Dr. Seamus Coveney,

Envo-Geo Environmental Geoinformatics, www.envogeo.ie Ireland

+353-053-9335940 seamus@envogeo.ie

Co-author: Mr. Kenneth Roberts,

Geographical and Earth Sciences, University of Glasgow, University Avenue, Glasgow G12 8QQ, United Kingdom.

44-0141-3306651 Kenny.Roberts@glasgow.ac.uk

Abstract

Digital Elevation Models generated from Unmanned Aerial Vehicle photogrammetry offer opportunities for on-demand DEM production in environmental modelling and flood risk prediction applications. The DEM and orthoimage accuracies that can be achieved using lightweight UAV on board sensors only, are compared with cases where progressively higher numbers of GNSS referenced ground targets are utilised. Unacceptably large 95% planimetric orthoimage errors of 5.22m (RMSE 3.27m), and DEM 95% elevation errors of 5.03m (RMSE 2.2m) are observed when using the on-board positioning and orientation sensors only. Introducing GNSS ground control points in increasing numbers progressively and substantially improves data accuracy. Remarkably small xy orthoimage errors of 0.076m (RMS) and DEM elevation errors of 0.08m (RMS) are achieved using 1 GCP for every 2 Ha of ground area and utilising more GCPs produced more or less identical results. These accuracies compare very favourably with the best commercial airborne survey DEMs, suggesting strong potential for the application of lightweight UAV photogrammetric DEMs in local environmental modelling and flood risk prediction applications. The potential of these DEMS for flood prediction is subsequently assessed and demonstrated by comparison with published flood risk maps and flood depth data, and by cross-comparing the outputs of the UAV DEM flood model predictions.

Keywords: UAV, UAS, RPAS, DEM & orthoimage accuracy; flood prediction.

1. Introduction

Digital Elevation Models (DEMs) from a range of remote sensing platforms are used widely for environmental modelling and flood prediction. Regional scale modelling of hydrological processes (Jarvis et al., 2008), erosion susceptibility (Verstraeten, 2006) and sea level rise vulnerability (Poulter & Halpin, 2008) can be achieved using small-scale DEMs derived from satellite imaging or high-altitude airborne photogrammetry. However, local large-scale spatial modelling of flood risk more often use DEMs derived from Synthetic Aperture Radar (García-Pintado et al., 2013) or increasingly, from bare-earth data derived from airborne Light Detection and Ranging (LiDAR) surveys (Haile & Rientjes, 2005).

The reliability of localised large-scale DEM-based environmental modelling is often heavily dependent upon DEM accuracy (Sanders, 2007; Horritt & Bates, 2002; Holmes et al., 2000). This is especially true in flooding applications, where relatively small elevation errors can result in significant horizontal flood prediction errors in shallow gradient flood-prone environments (Sanders, 2007; Bates & De Roo, 2000). The importance of elevation accuracy is recognised in flood prediction studies that utilise DEMs in river flood risk prediction (Cobby et al.,2001) urban coastal flood sensitivity mapping (Kulkarni et al., 2014) and the spatial prediction of vulnerability to sea-level rise risk (Coveney & Fotheringham, 2011a).

The elevation accuracies that can be achieved using bare-earth LiDAR Digital Terrain Model (DTM) data tend to make it the preferred data source for local scale flood modelling studies. However, high acquisition costs still often limit geographical coverage in many contexts. Airborne SAR DEM data are frequently used in these circumstances (García-Pintado et al., 2013, Coveney, 2013a) and Terrestrial Laser Scanning (TLS) can offer a good alternative for smaller areas (Heritage & Large, 2009) where dense ground vegetation is absent (Coveney & Fotheringham, 2011b). Good quality DTMs may also be generated for smaller areas from GNSS survey data, particularly in areas of non-complex terrain where high-density ground sampling may not be required (Coveney et al., 2010).

The potential to generate on-demand photogrammetric DEM data from UAV photogrammetry (Remondino et al., 2011) is providing new opportunities for DEM-based environmental modelling and flood prediction (Leitão et al., 2016). Falling costs for lightweight UAV / Unmanned Aerial Systems / Remotely Piloted Aerial Systems (Bürkle et al., 2011) and the increasing affordability and ease of use of photogrammetric processing software (Küng et al., 2011) are likely continue to drive growing demand for UAV photogrammetric DEM products. This is increasing the uptake of UAVs / Unmanned Aerial Systems (UAS) / Remotely Piloted Aerial Systems (RPAS) among non-specialist users who are primarily concerned with the suitability of off-the-shelf lightweight systems in environmental applications (Anderson & Gaston, 2013). Evolving applications for UAV DEMs include river flood risk prediction (Serban et al., 2016; Tamminga et al., 2015) urban mapping (Unger et al., 2014) and coastal modelling studies (Klemas, 2015; Darwin et al., 2014).

This is leading to an increased focus on the issue of UAV data accuracy. Examples include assessments of UAV orthoimage accuracy (Darwin et al., 2014; Küng et al., 2011), which indicate that sub-decimetre horizontal errors are attainable using light weight UAV systems. Research that considers the accuracy of UAV-derived DEMs employs a variety of approaches. UAV elevation accuracies of the order of ±0.3m are reported when using total station validation data (Serban et al., 2016; Udin & Ahmad, 2014). Studies that validate UAV DEM accuracy with external high accuracy DEM data (Unger et al., 2014) including LiDAR (Leitão et al., 2016) report that UAV DEM performance may be competitive with LiDAR. Some research studies highlight elevation differences of the order of ±0.3m between UAV DEMs and the input ground control points used in the photogrammetric process (Vallet et al., 2011). However, even smaller elevation errors are noted by authors that have used substantial numbers of GNSS survey ground control points (Tamminga et al., 2015; Uysal et al., 2015). Tamminga et al, (2015) use approximately 1.5 GCPs per hectare and 7 check points per hectare, achieving very impressive UAV DEM RMS elevation errors of ±0.088m on a substantially un-vegetated gravelled river course. Uysal et al. (2015) achieve even more impressive RMS elevation accuracies of ±0.066m, using 6 GCPs and 6 separate check points per hectare on a substantially

unvegetated upland survey site.

The combined results of all of the published research suggests that UAV DEM data and orthoimage data can meet the needs of the majority of environmental applications to which growing numbers of non-specialist UAV users wish to apply them. This paper seeks to provide a detailed assessment of the range of UAV DEM and orthoimage accuracies that can be achieved with and without ground reference data, and when differing numbers of ground reference points are employed in the photogrammetric process. The results of these empirical tests are subsequently applied to assess the potential for UAV photogrammetric DEMs to be usefully applied to an environmental modelling application that requires very high accuracy DEM data in order to provide meaningful results; namely the spatial prediction of river flood risk. The flood model assessment is intended primarily for demonstration purposes, and is not proposed as an alternative to published risk maps. Comparison with published data is intended to demonstrate the potential of UAV DEM data for environmental modelling and flood prediction, in situations where no other suitable DEM data are available.

The following specific questions are addressed:

1. What orthoimage and DEM accuracies can be achieved without using exterior GNSS ground referencing data

2. What improvements in DEM and orthoimage accuracy can be achieved using progressive numbers of ground reference points

3. Do these DEMs offer potential for the spatial modelling of flood risk.

2. Methodology

2.1 Site selection

The chosen survey site (Figure 2a and 2b) was selected to try to maximise the potential to evaluate data accuracy, and to make the results transferable to a range of other environmental contexts also. Firstly, the site needed to be sufficiently large to accommodate the 500m radius limits that are allowable (CAA, 2016) for line of sight operation. Second, in order to test DEM accuracy, the chosen area ideally needed to be characterised by some variability in ground elevation and terrain slope. Thirdly, a suitable candidate area needed to provide sufficient open areas to place GNSS-referenced ground targets at roughly similar horizontal separations at ground level. It was also desirable that chosen area should present a mix trees, bushes, ground vegetation, buildings and other 3D features to evaluate the degree to which the detail of 3D features were realistically represented in the DEM data outputs. Lastly, because flood modelling was judged in advance to be a suitable method to compare the relative performance of DEMs generated using differing levels of ground control data, the site needed to include a river that was subject to flooding and overflow. A suitable area was found in an urban parkland area in the city of Glasgow in Scotland (Figure 2).

2.2 Data acquisition

2.2.1 UAV data

The aerial survey was carried out using a SenseFly Swinglet CAM UAV (Figure 1). Swinglet CAM is a lightweight (500gram) delta wing platform with a wingspan of 80cm that is designed for autonomous mapping applications (SenseFly, 2011). It is powered by swappable lithium polymer batteries that drive an electric motor and push mode propeller. It is capable of approximately 20 minutes of flight, and is automatically limited to fly within the legally-permitted 500m radius and maximum height limit of 100m

above its launch location.

Figure 1: Schematic of Swinglet Cam UAV (Source: SenseFly, 2011).

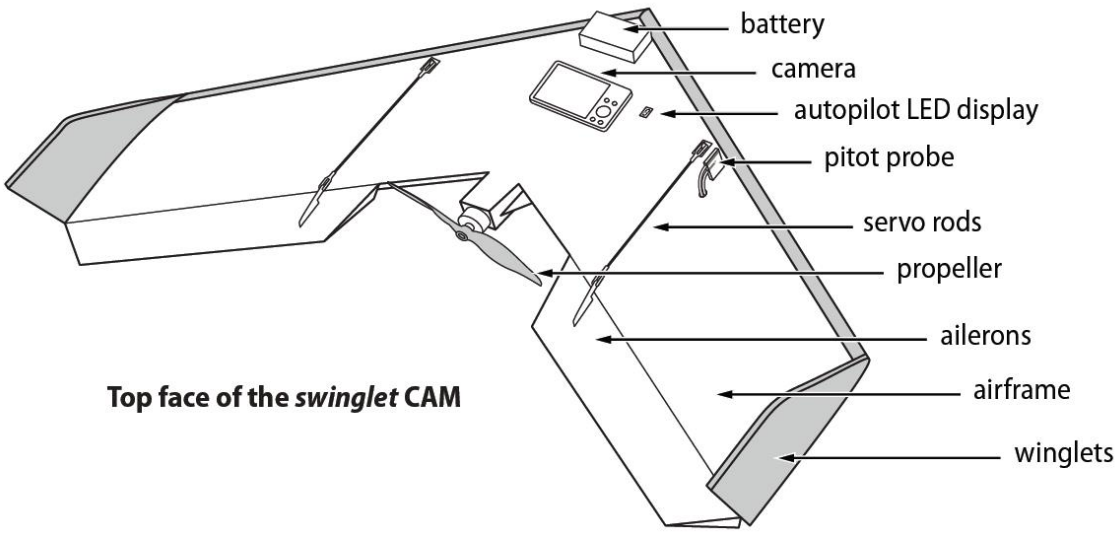

2.2.2 UAV sensors

The supplied camera is a modified Canon Ixus 120IS 12 Megapixel RGB camera that mounts through the airframe body (Figure 1). The camera charge coupled device (CCD) acquires 4000 x 3000 pixel images at a pixel size of 1.54 µm. The UAV uses a single-frequency (u-BLOX) GPS chip, recording airframe x,y,z coordinates (C/A code only) at each photo location. The pitch, roll and yaw of the UAV are recorded for each image event using an integrated Microelectromechanical system (MEMS) Inertial Measurement Unit (IMU). Autonomous flight is managed by an on board Flight Management System which is radio linked to a survey laptop on the ground via a 2.4 GHz modem unit (SenseFly, 2011).

2.2.3 External GNSS Ground data

A Leica Geosystems Viva GS08 NetRover GNSS receiver was used to define the xyz positions of 61 ground targets (Figure 3) that were fixed in position immediately before the flight. The GS08 is a 72 channel unit, tracking signals from GPS (L1, L2 & L2c) and GLONASS (L1, L2) satellites. The survey was undertaken in rover mode, accessing Realtime Kinematic (RTK) positioning corrections via 4G using the Leica SmartNet service (SmartNet, 2016). Accuracy statistics issued by SmartNet indicated that 95% of horizontal positioning errors in the external GNSS data set were ±0.005m, 95% of elevation errors were up to ±0.011m, and the maximum elevation error in the external GNSS reference data was 0.026m. The GNSS defined xyz positions of the ground targets were later used for the DEM and orthoimage generation, and to validate their accuracy.

2.3 Survey design

2.3.1 UAV survey design

The survey area was comprised of 29 Ha of urban parkland in the City of Glasgow, Scotland in the United Kingdom (Figure 2b). A survey plan was set up using the SenseFly E-motion software, specifying a minimum image endlap & sidelap of 80%, with no segment of the survey extending outside a 500m line of sight radius from the intended flight launch point. E-motion automatically defined the flight survey waypoints based upon the dimensions of the survey area and the user-defined image overlaps. The E-motion

installation on the survey laptop allowed for modifications of any aspect of survey design that might be required at survey time.

Figure 2: (a) Site location context map, and (b) Site detail map, (c) flight track map showing image sequence numbers and start and end points for flight at image number 38.

(a) Site Location and context map (b) Site detail map (c) Flight track

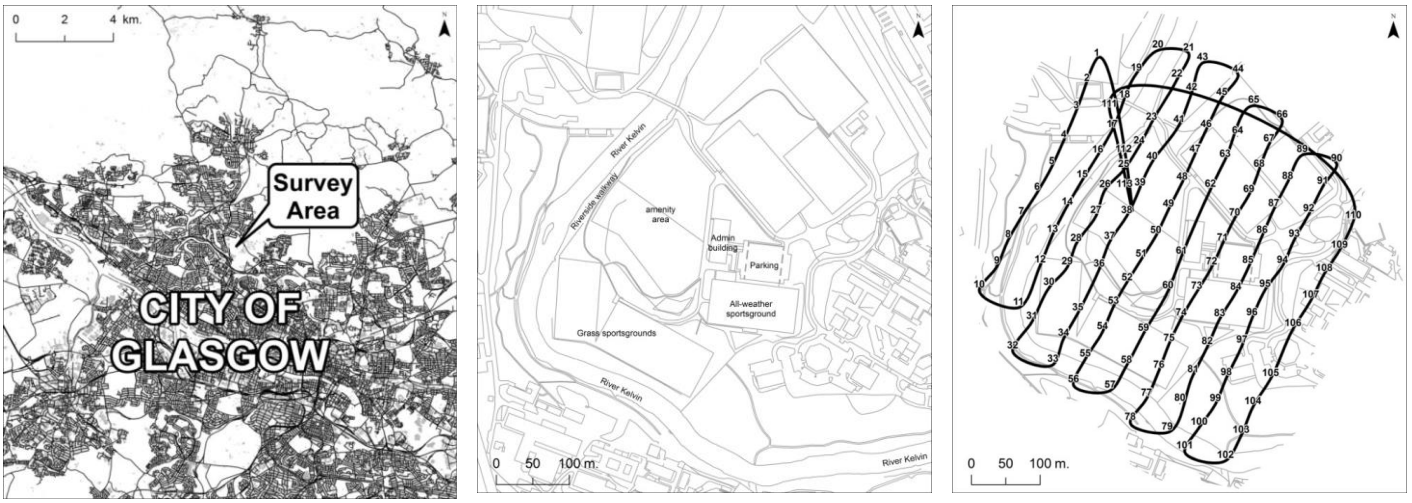

2.3.2 GNSS ground survey design

A positioning plan was set up for the placement of 61 high-contrast ground targets (Figure 3) that were used later to introduce external RTK GNSS xyz spatial referencing for orthoimage and DEM production. The planned locations of these ground targets were selected to provide up to 2 ground target referencing points per hectare. Subsets of the full ground target set were later used to introduce successively larger numbers of ground control points (GCPs) for DEM and orthoimage generation (Figure 3) and accuracy testing.

2.3.3 Ground target installation

The ground targets consisted of 20cm x 20cm black and white 4-panel checkerboard grids printed and laminated at A4 size. These were nailed to the ground surface at the locations outlined in the target plan immediately before the aerial survey. The xyz coordinates of the centre points of the in-situ targets were then re-surveyed with the Leica GS08 GNSS receiver, generating a set of high accuracy xyz coordinates for all 61 target locations (Figure 3).

Figure 3: Ground Control Point sets used in DEM and Orthoimage generation. The 61 GCP set was also used for ground target placement.

5 GCP set

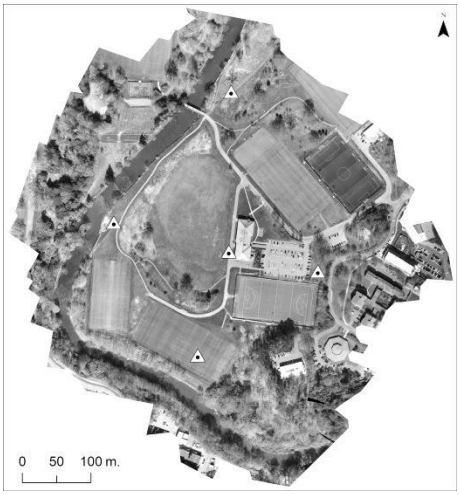

10 GCP set

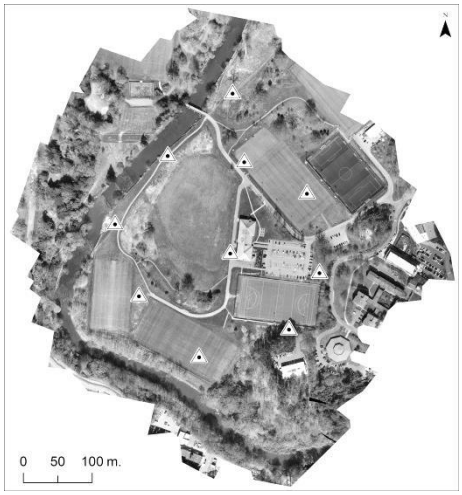

15 GCP set

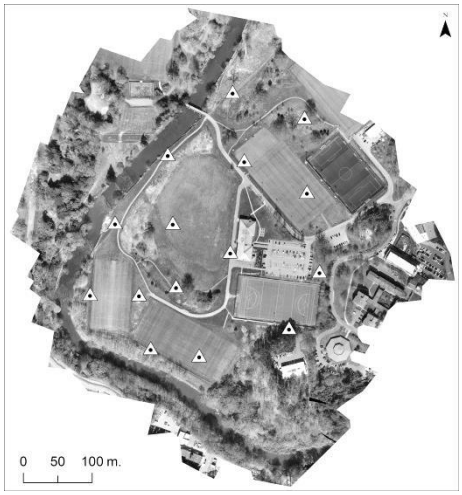

30 GCP set

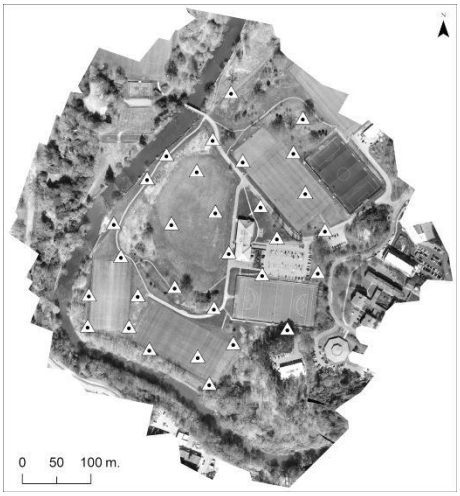

45 GCP set

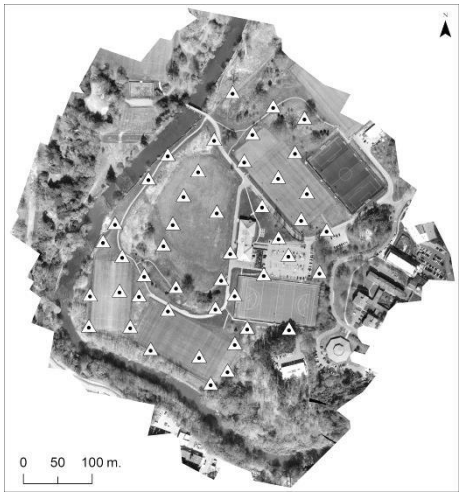

61 GCP set / initial GCP Plan

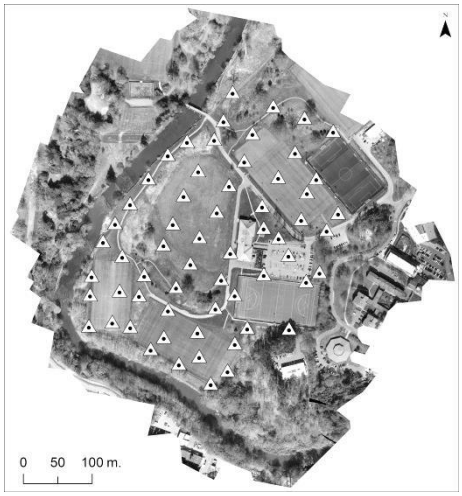

2.4 Surveys

2.4.1 Swinglet CAM survey

Flight parameters were set and managed using the SenseFly E-motion software module. A final flight track was automatically generated in E-motion (Figure 3), based upon user-defined survey extents and specified image endlaps and sidelaps of 80%. A maximum flying height of 90m above launch height was selected, generating a ground pixel size of approximately (variations in the height of the ground surface across the survey area affected final pixel sizes) 3.5 cm x 3.5cm.

The UAV was launched from an open grassed area, coincident with the location of image 38 (Figure 3). The flight was run in fully autonomous mode, climbing to 90m above the launch height before proceeding to follow the pre-defined flight track. E-motion managed the timing for image acquisition to achieve the specified minimum overlaps, momentarily switching off power to the propeller to reduce vibration in advance of acquiring each image in glide mode. The final image set was comprised of a set of 120 overlapping images (Figure 2c). Each image was automatically tagged with unique image identifiers and time stamps, which were used during photogrammetric processing. The full survey was competed in 11 minutes, returning autonomously to circle the launch point and glide back to ground under control from E-

motion.

2.5 Photogrammetric processing

Photogrammetric processing was carried out using Agisoft PhotoScan Professional (1.1). The survey images were loaded into PhotoScan along with the respective GPS and IMU text data that were recorded by E-motion for each survey image. These data were used to assign camera locations in PhotoScan, forming the basis of a block adjustment. The relevant camera parameters for the Canon Ixus 120IS were added to the adjustment from the pre-defined camera list in PhotoScan. PhotoScan uses a Structure from Motion (SfM) approach, employing a Scale Invariant Feature Transform (SIFT) algorithm to generate tie-points for feature matching at image overlaps. It computes pair-wise depths from the camera positions to generate an orthoimage and a DEM (Agisoft, 2016). Therefore, it allows for the generation of orthoimage and DEM products using internal positioning, orientation and SfM only. However, it is assumed that users will introduce external GNSS GCPs when higher accuracies are required (Agisoft, 2014). The software provides a text import facility to introduce external GNSS orientation data into the adjustment process.

The xyz GNSS ground target coordinates were imported into PhotoScan and interactively assigned to the centres of each of the high-contrast ground targets as they appeared on each of the 120 non-mosaicked images. A new orthoimage and DEM was produced for each of six subsets of the full 61 GCP set. These subsets consisted of: 5, 10, 15, 30, 45 and 61 GCPs. This progressive introduction of additional GCPs was undertaken in order to demonstrate the orthoimage and DEM accuracies that were achievable using differing numbers of ground control points. This information may be of interest to those who are considering the use of UAV DEM data in environmental modelling applications, helping to approximate the numbers of GCPs that may typically be required to achieve the accuracy required for a given application. The spatial distribution of each GCP subset was selected to achieve an approximately equal separation in each case (Figure 3). Successive subsets encapsulated the previous set, adding further GCPs to that set. In total (including the orthoimage and DEM that were generated using interior orientation) this produced a final tally of seven sets of orthoimages and DEMs. The accuracies of these were quantified in PhotoScan, with some additional external checks being performed in ArcGIS 10.2.

3. Data accuracy assessment

As noted previously, the validity of environmental models that are based on DEM data are generally strongly related to the accuracy of the DEM data sets upon which they are based. The accuracies that were achieved using internal positioning and orientation, were compared with what could be achieved using successive numbers of external GNSS-referenced GCP data. DEM elevation accuracies were of primary interest, because of their important role in modelling environmental processes such as those that are discussed in the Introduction. However, since many UAV users may be more concerned with orthoimage accuracy, these are considered also.

3.1 Accuracies achieved using internal orientation only

3.1.1 Orthoimage

The zero-GCP orthoimage appeared at first glance to achieve generally good horizontal accuracies, but even a visual comparison of feature edges with national mapping agency 1:10,000 vector data indicated that some horizontal errors were apparent. (Figure 4). PhotoScan produces estimates of camera position errors only when no GCPs or check points are introduced, so the horizontal orthoimage errors were externally checked in ArcGIS 10.2. The centre coordinates (British National Grid projection) of the ground targets were digitised from the zero GCP orthoimage mosaic in ArcMap (Figure 4) and the x, y and

combined xy offsets were determined relative to GNSS-defined positions of all 61 ground targets. Offsets were measured using the ArcGIS Point Distance tool. X-direction errors ranged from 4.08m to -2.08m, and Y-direction errors ranged from 5.48m to -1.49m (Table 1). The X direction, Y direction, and combined XY errors were somewhat smaller in the northern portion of the survey area, where the UAV was launched from. Errors were larger elsewhere (Figure 4). This may have been related to a height difference between the northern half, and lower elevations in the southern portion of the site (Figure 4). Orthoimages that subsequently used GCPs did not display this characteristic.

Figure 4: Horizontal errors in the zero GCP orthoimage.

(a) X direction errors (m)

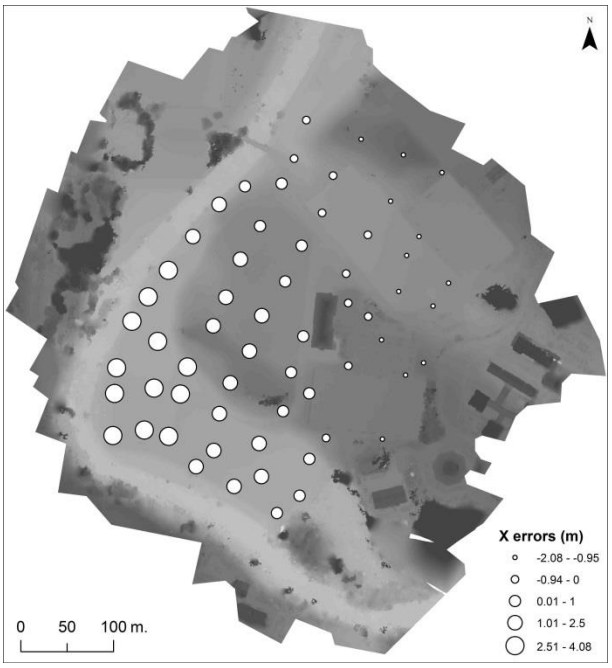

(b) Y direction errors (m)

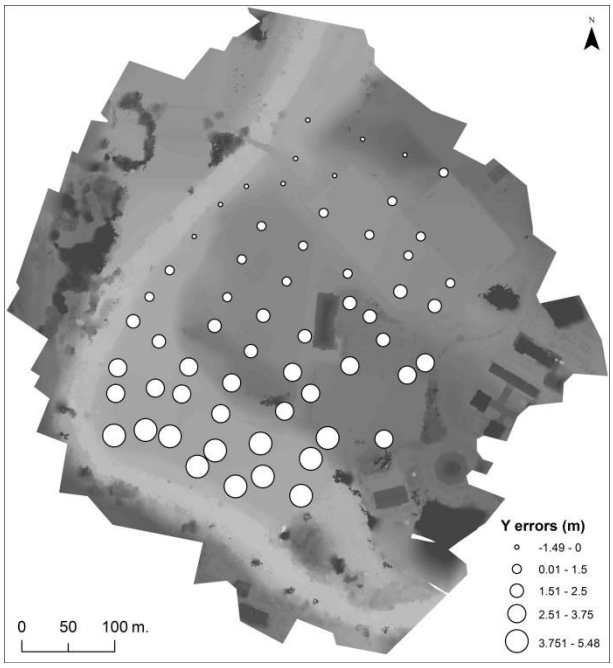

(c) Combined XY errors (m)

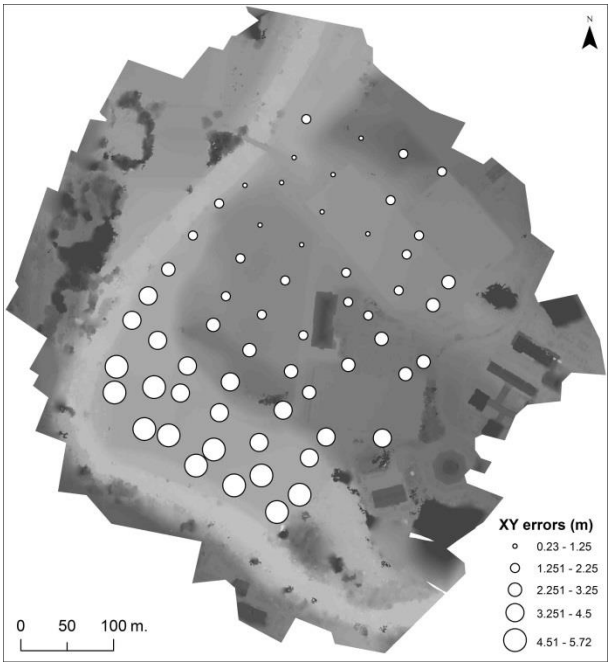

(d) 61 GCP ortho and 1:10,000 vector overlay

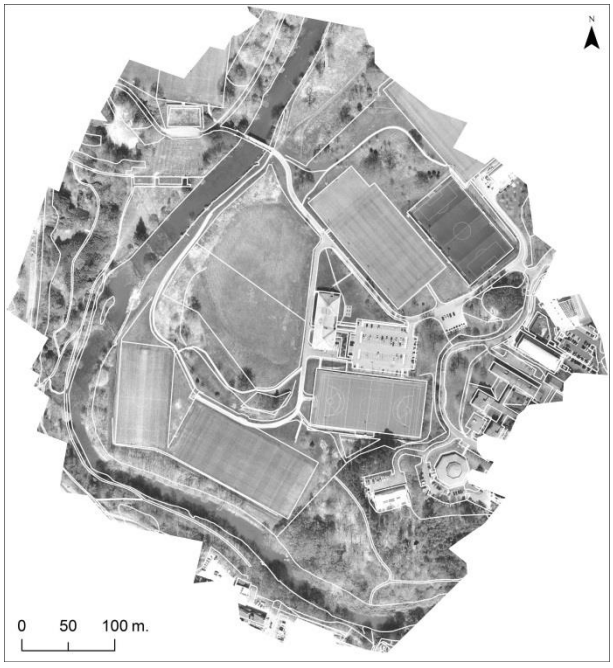

3.1.2 DEM

DEM elevation errors in the zero GCP DEM were quantified in ArcGIS 10.2 using the 'Extract values to points' tool in ArcToolbox. Elevation differences between the DEM surface and external GNSS ground-target (GCP) coordinates were large, ranging up to 5.82m, and 95% of these errors were ≤5.03m. The overall RMS elevation error was 3.267m (Table 2). These results suggested that the zero GCP DEM might be of little value for modelling any environmental process that is dependent upon elevation, including flood modelling.

3.2 Accuracies achieved using external GNSS control

3.2.1 Orthoimage accuracy

PhotoScan provided maximum and mean x and y error statistics only, so ArcGIS was used to provide additional accuracy statistics for the 0GCP 15GCP and 61 GCP orthoimages (Table 1). These three GCP sets represented the minimum, maximum and the optimal numbers of ground control points used for orthoimage generation. Maximum and mean horizontal errors in the 5 GCP orthoimage were (respectively) 0.31m and 0.28m, and maximum and mean horizontal errors (respectively) in the 10 GCP orthoimage were 0.28m and 0.14m. Similar maximum and mean horizontal errors were reported by PhotoScan for all the other orthoimages (Table 1). ArcGIS offered a range of descriptive statics that were not available in PhotoScan, so the 15 GCP orthoimage was double-checked in ArcGIS. Very slightly larger errors were noted in ArcGIS, but a 95% of combined xy positioning errors were ≤0.11m and RMS error were as low as 0.08m (Table 1). The accuracy of the 61 GCP orthoimage was double-checked in ArcGIS also, indicating that adding a further 45 GCPs made essentially no difference to the accuracy of the resulting orthoimage. In this case, 95% of combined xy positioning errors again at ≤0.11m, and RMS positioning errors reduced very slightly to 0.07m (Table 1).

Table 1: Agisoft PhotoScan (& ArcGIS**) validation results (x & y only) for all seven Orthoimages. Results from Agisoft include residual horizontal errors (in italics) at GCP point locations.

Agisoft PhotoScan	*Ortho 0 GCPs* **	Ortho 5 GCPs	Ortho 10 GCPs	Ortho 15 GCPs	*Ortho 15 GCPs* **	Ortho 30 GCPs	Ortho 45 GCPs	Ortho 61 GCPs	*Ortho 61 GCPs* **
Validation points:	*61*	5 + 56	10 +51	15 + 46	*15 + 46*	30 + 31	45 + 16	61	*61*
Max pos. X error:	*4.081*	-	0.278	0.233	*0.29*	0.252	0.298	0.270	*0.288*
Max neg. X error:	*-2.079*	-0.311	-	-	*-0.07*	-	-	-	*-0.087*
Mean X error:	*0.773*	0.279	0.138	0.060	*0.01*	0.066	0.064	0.061	*0.006*
Max pos. Y error:	*5.482*	0.279	0.253	-	*0.11*	-	-	-	*0.12*
Max neg. Y error:	*-1.495*	-	-	-0.139	*-0.235*	-0.164	-0.187	-0.196	*-0.24*
Mean Y error:	*2.025*	0.182	0.114	0.071	*0.004*	0.043	0.041	0.041	*0.007*
Max xy error	*5.72*	-	-	-	*0.34*	-	-	-	*0.32*
Mean xy error	*2.90*	-	-	-	*0.046*	-	-	-	*0.05*
95% xy error	*5.22*	-	-	-	*0.11*	-	-	-	*0.11*
RMSE xy error	*3.265*	-	-	-	*0.076*	-	-	-	*0.074*

3.2.2 DEM accuracy

As noted previously, the reliability of DEM-based environmental models is reliant on DEM elevation accuracy. This is particularly so for flood modelling, where even relatively small DEM elevation errors can result in substantially erroneous predictions of potential horizontal flood in shallow-gradient contexts (Sanders, 2007; Bates & De Roo, 2000). The DEMs generated using zero, 5, 10, 15, 30, 45 and 61 GCPs were validated using the full set of 61 GCPs. Including all 61 GCPs provided a more comprehensive measure of actual DEM elevation errors, especially in cases where a large number of GCPs were used and the number of available hold-out points was substantially reduced. ArcGIS 10.2 also provided a greater range of statistical measures of DEM accuracy than was available in PhotoScan, and constituted a useful double-check also.

DEM elevation errors (Table 2) were quantified in ArcGIS 10.2 by extracting the PhotoScan DEM elevation values to the 61-point GCP coordinate points using the ArcGIS 'extract values to points' tool. As noted briefly previously, the zero GCP DEM was characterised by very large errors, ranging from +0.67m to -5.15m, suggesting the this DEM would not be suitable for use in environmental modelling applications. The additional 95% elevation error statistic of 5.03m, and the RMS elevation error of 2.2m highlighted in ArcGIS (Table 2) supported this conclusion. The zero GCP DEM also failed to represent most of the topographical detail, apart from a few of the very largest features. Contouring the elevation errors in this DEM demonstrated the magnitude and overall distribution of these elevation errors (Figure 5).

The DEM generated using 5 GCPs (approximately 1 GCP for every 6 Hectares) was characterised by 95% of elevation errors ranging to ≤3.88m, and an overall RMS elevation error of 1.31m (Table 2). The 10 GCP DEM performed substantially better, with 95% of elevation errors of ≤1.38m and an RMS elevation error of 0.34m (Table 2). While these results represented improvements over the zero GCP DEM, they were still quite large. However, very substantial accuracy improvements were observed in the 15 GCP DEM (approximately 1 GCP for every 2 Hectares) where 95% of the elevation errors were ≤0.20m and RMS elevation error was 0.08m (Table 2). This RMS error was about as good as was noted in similar studies that used slightly larger numbers of GCPs (Tamminga et al., 2015; Uysal et al., 2015).

Larger numbers of GCPs were introduced for the generation of successive DEMs to see if further accuracy improvements were achievable. However, the DEMs generated using 15, 30 GCPs (c.1 per Ha.), 45 GCPs and 61 GCPs (c.2 GCPs per Ha.) demonstrated almost identically low 95% and RMS elevation errors (Table 2). Therefore, increasing the number of GCPs beyond 15 GCPs (approximately 1 per for every 2 hectares in this case) offered no additional benefits. Furthermore, the representation of features including buildings, parked cars, isolated trees and bushes (Figure 5) were also equally well represented in all the DEMs generated using 15 or more GCPs. Contour visualisations of elevation error revealed very similar spatial distributions of elevation error among these DEMs also (Figure 5).

It is important to note that these DEM accuracies are comparable with the accuracies that are commonly achieved when using airborne LiDAR (Sibona et al., 2016; Tulldahl et al., 2015, Coveney 2013a, Hodgson, M. E., & Bresnahan, 2004). The capacity of lightweight UAVs to provide data accuracies that compare favourably with airborne LiDAR may be of interest to DEM data users that require accurate DEM data for application in local environmental modelling studies, including flood modelling, in situations where LiDAR data are not available. The results of the empirical accuracy evaluations were conclusive, confirming the likely potential for GNSS-survey controlled UAV-derived photogrammetric DEMs to be applied as the basis for flood prediction modelling in similar contexts elsewhere. No published flood records were available that could be used to directly validate flood model outputs. However, it was possible to assess and demonstrate the performance of the UAV DEM flood prediction models by comparing them with the best available published flood risk maps (SEPA, 2016b) and flood depth records (SEPA, 2016a). It was also possible to assess the relative performance of each UAV-DEM for the prediction flood risk by cross-comparing modelled flood predictions.

Table 2: ArcGIS validation results (elevation only) for all seven Digital Elevation Models that were generated for comparative purposes.

ESRI ArcGIS	DEM using 0 GCPs	DEM using 5 GCPs	DEM using 10 GCPs	DEM using 15 GCPs	DEM using 30 GCPs	DEM using 45 GCPs	DEM using 61 GCPs
GCPs per Hectare	-	0.17	0.34	0.51	1.03	1.54	2.09
Validation points:	61	61	61	61	61	61	61
Max positive elevation error	0.67m	2.11m	0.22m	0.32m	0.30m	0.23m	0.22m
Max negative elevation error	-5.15m	-2.73m	-1.21m	-0.18m	-0.25m	-0.26m	-0.40m
Mean elevation error	-1.67m	0.28m	-0.12m	-0.04m	-0.04m	-0.04m	-0.05m
Std. Dev. Elevation error:	1.43m	1.28m	0.32m	0.06m	0.07m	0.06m	0.07m
Total error range (z):	5.82m	4.84m	1.44m	0.50m	0.55m	0.50m	0.62m
95% error range (z):	5.03m	3.88m	1.38m	0.20m	0.19m	0.19m	0.21m
RMSE (z):	2.20m	1.31m	0.34m	0.08m	0.08m	0.08m	0.09m

Figure 5: DEM errors visualised as error contours for all seven DEMs.

(a) 0 GCP DEM

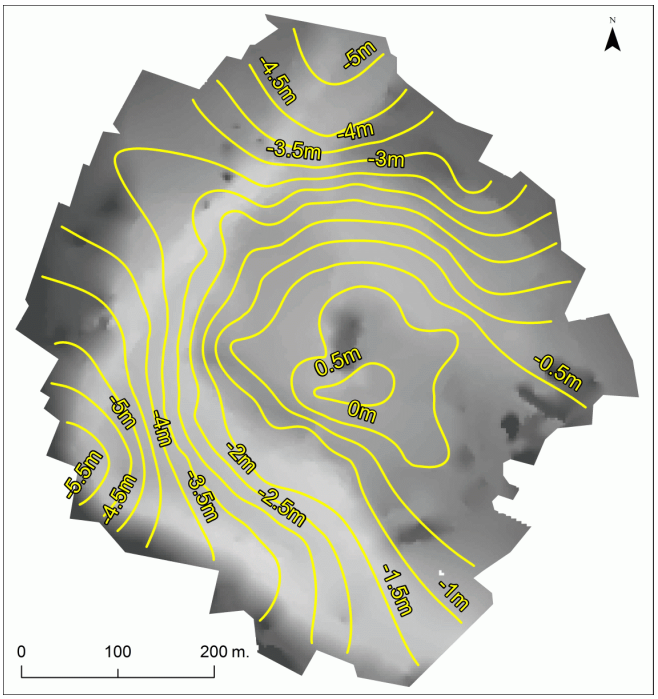

(b) 5 GCP DEM

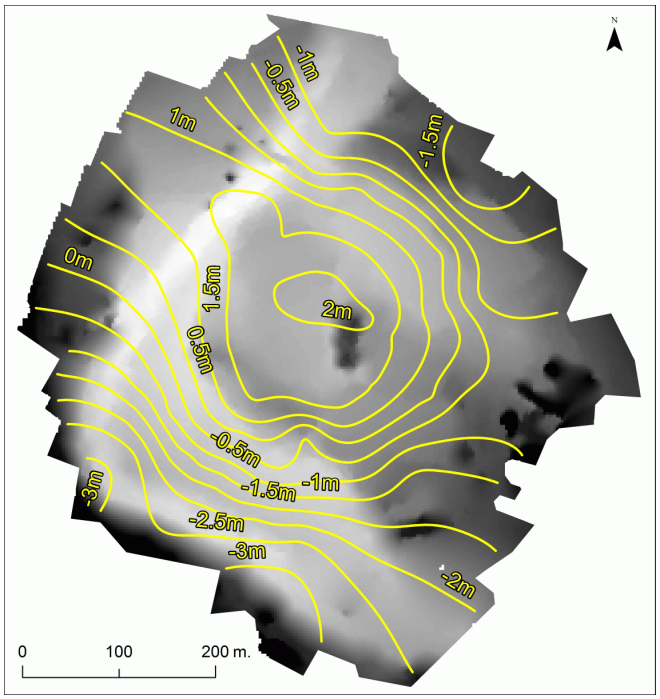

(c) 10 GCP DEM

(d) 15GCP DEM

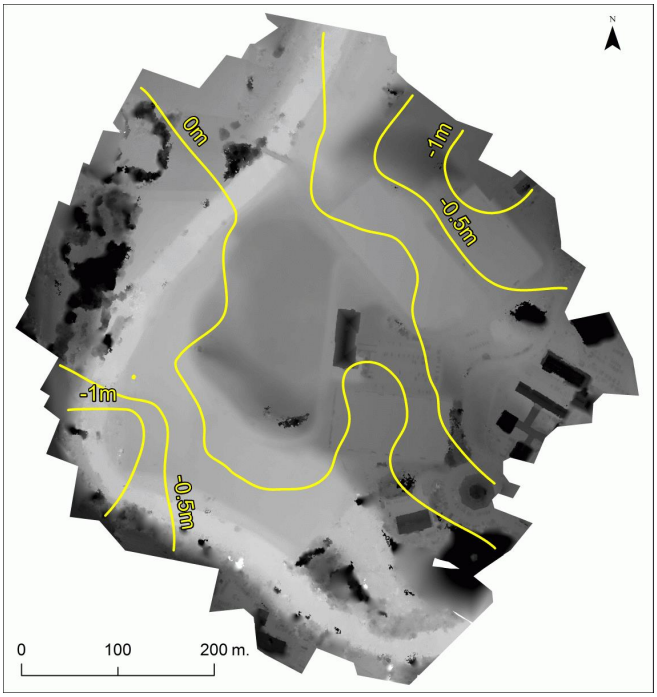

(e) 30 GCP DEM

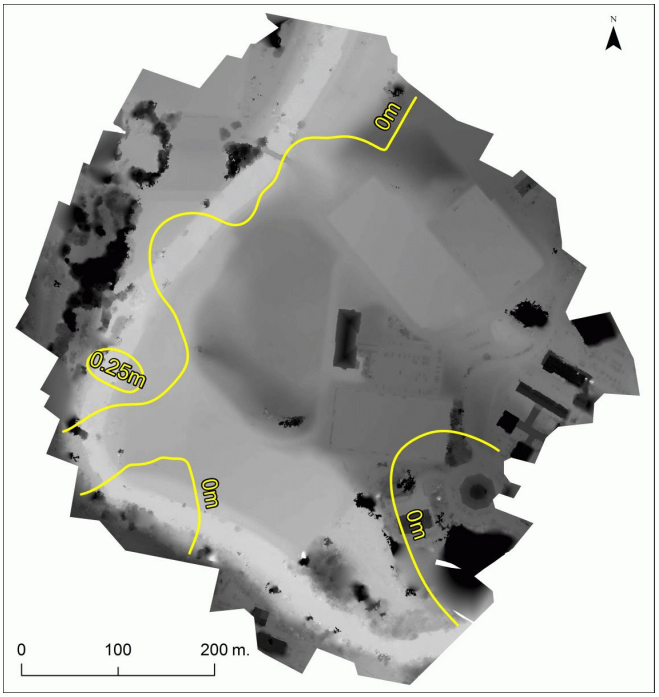

(f) 45 GCP DEM

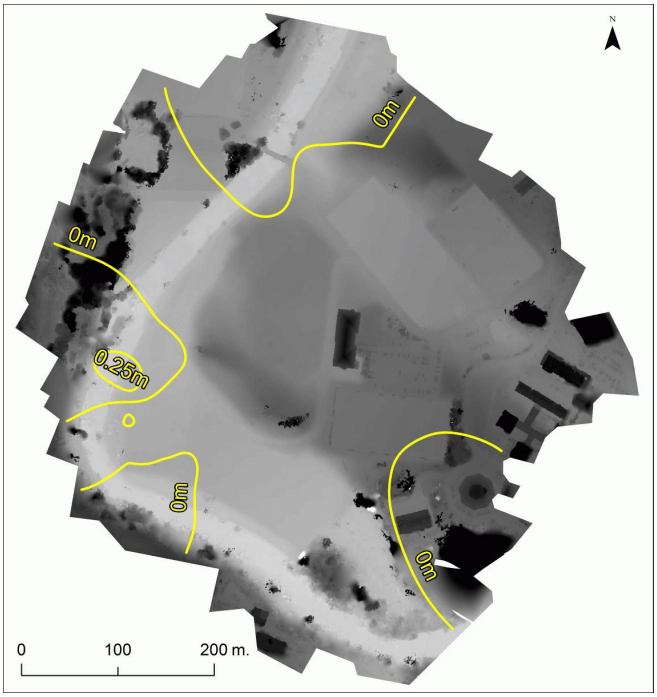

(g) 61 GCP DEM

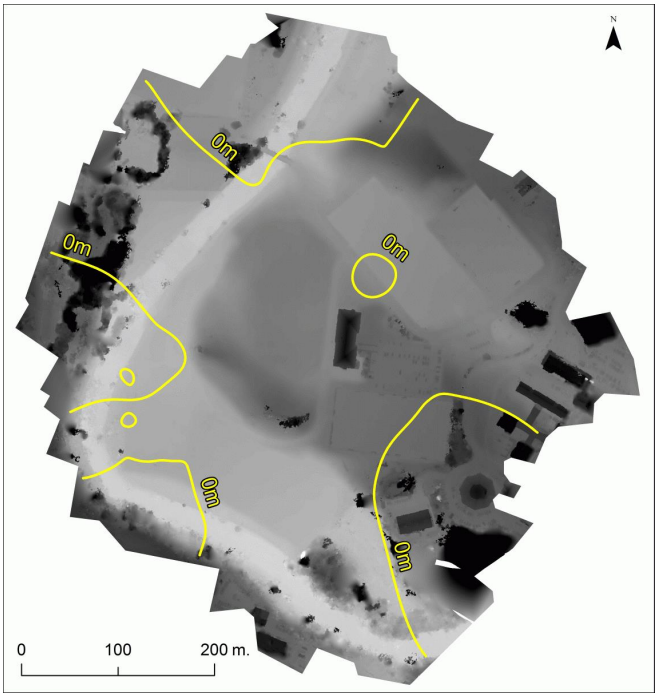

(h) 61 GCP Orthoimage

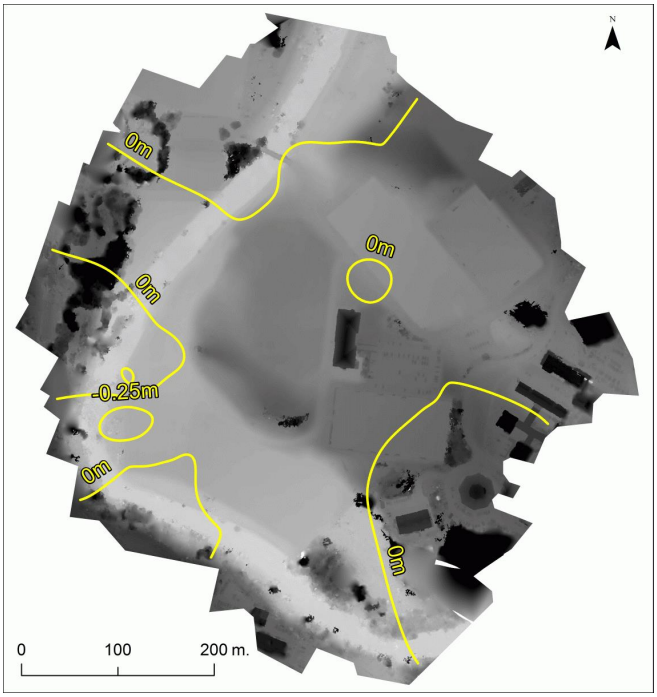

3.3 Flood prediction assessment

Inundation risk zones were delineated by reclassifying DEM raster elevation values into flood risk categories that are based upon the elevation of recorded or potential flood heights. This approach is used by the Scottish Environmental Protection Agency (SEPA, 2015) to generate flood risk maps for all of Scotland, including the study area that was used for this study (Figure 2). SEPA delineates DEM raster cells on its combined airborne LiDAR / airborne Synthetic Aperture Radar data (SEPA, 2015) into high, medium and low flood risk categories (Figure 7). Flood depths that are attached to these risk categories, and flood risk maps are published as interactive maps online, utilising medium resolution topographic maps that provide locational context (SEPA, 2016b). The potential for the UAV DEM data to be used to meaningfully model flood risk are assesses relative to these SEPA risk maps and SEPA (text-based) flood depth data records.

It is important to note that the UAV DEM flood predictions are not suggested as alternatives to existing published risk maps. Rather, they are presented here to demonstrate the potential of UAV DEM data to be used to model flood risk in a meaningful manner, especially in situations where suitable DEM data are not available. The reader is directed to the preceding sections, where the evaluation of UAV DEM accuracy provides some empirical evidence of its potential suitability for use in flood prediction applications.

The flood prediction assessment involved the following:

1. Comparison with SEPA flood risk maps and recorded flood depths
2. Inter-comparison of the UAV DEM flood predictions, assessing the degree to which they predict similar flood risk extents

Comparison with available flood data sets

Flood records from the Scottish Environmental Protection Agency (SEPA) river flood gauge at Killermont

(Figure 6) were used as reference data. The Killermont river level gauge is located less than 1km from the study area (Figure 8), and this provided a published set of annual flood maxima records (SEPA, 2016a) that extended from 1948 to 2005 (Figure 6). These data were used to evaluate the flood depths that were associated with the non-numeric SEPA low-risk, medium-risk and high flood risk categories. SEPA do not publish the flood depths for each flood risk category, but it was possible to infer these from the published annual maximum flood depths at Killermont (Table 3, Figure 6). This enabled a comparison to be made between the published SEPA risk maps (which constitute the best-available published data regarding flood extents) and the UAV DEM prediction maps. The SEPA flood high, medium and low flood risk categories (Figure 7) matched very closely with 1-metre above normal flood levels, the largest flood depth recorded at Killermont between 1948 – 2005, and 0.5 metres above this (1994) annual flood maximum (Table 3). The inferred flood risk heights were then used to delineate comparator flood risk zones using the UAV DEM data (Figure 7). These resulting flood zones were similar to the flood risk areas in the SEPA flood risk maps (SEPA, 2016b), which suggested that the UAV DEM data sets provided a reasonable basis for reliable flood prediction.

Figure 6: Maximum annual flood height (in metres) recorded at the Killermont flood level gauge (SEPA, 2016a).

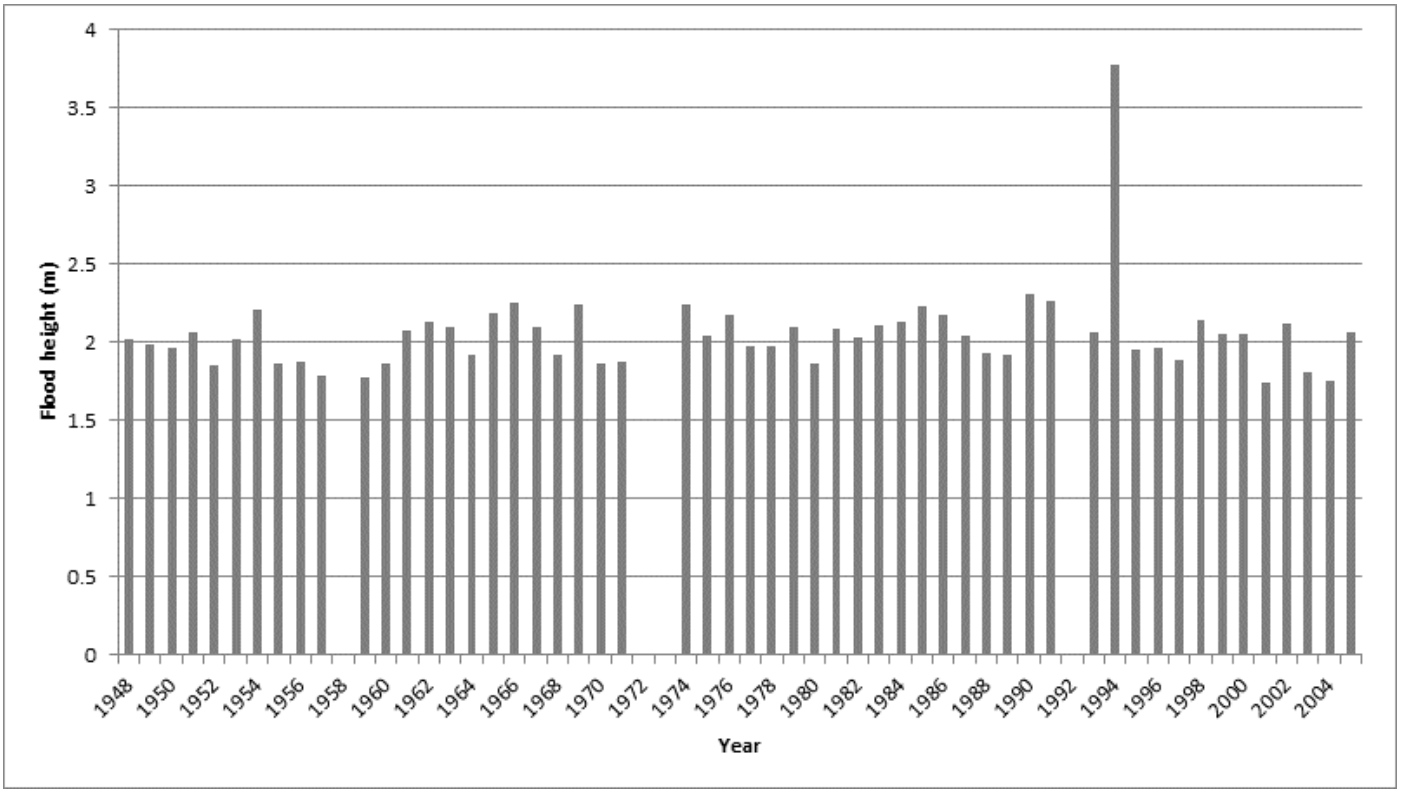

Table 3: Summary statistics for maximum annual flood depths at Killermont river level gauge, and inferred flood depths for the SEPA descriptive flood risk categories.

Flood gauge level	Level (m)	SEPA flood risk category	lower (m)	upper (m)	Description
Normal	27.24	-	-	-	Normal river level at Killermont 1948-2005
Average	27.55	-	-	-	Average flood level at Killermont 1948-2005
-	-	High flood risk	-	28.55	1 metre above average flood level at killermont
-	-	Medium flood risk	28.56	-	Lower bound of medium flood risk category
Maximum	29.28	Medium flood risk	-	29.3	Maximum flood event recorded at Killermont (1994)
		Low flood risk	29.31	-	Lower bound of low flood risk category
		Low flood risk	-	29.8	Upper bound low risk (+0.5m max 1994 flood)

Figure 7: Flood models delineating SEPA high, medium and river flood categories (a) modelled using the 15-GCP UAV DEM, and (b) as delineated in SEAP flood risk mapping.

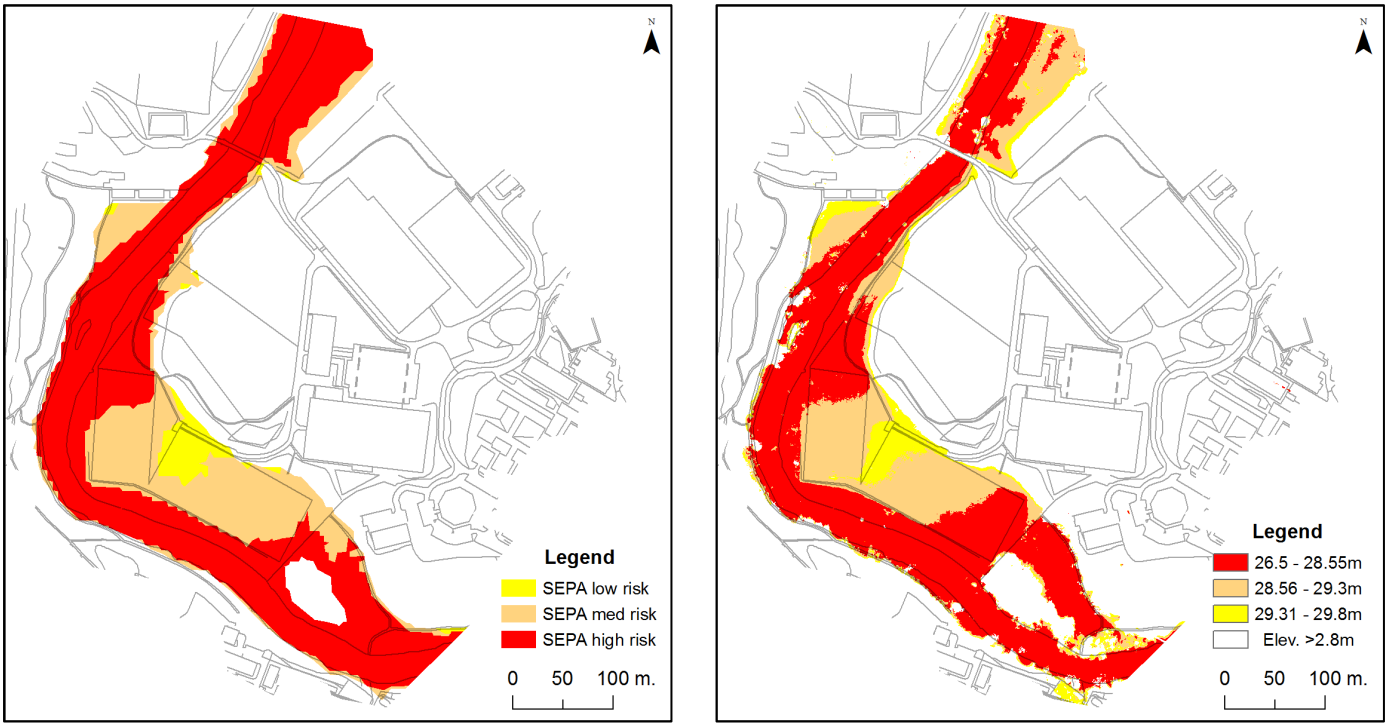

It is important to stress at this juncture that the DEM data used by SEPA as the basis of their flood prediction maps are themselves flood prediction models that are derived from a mixture of airborne LiDAR and airborne Synthetic Aperture Radar (SAR) data (SEPA, 2015). The spatial resolution of these data ranges from 5-metres to 10-metres in lowland areas of Scotland, up to 20-metres in upland areas (SEPA, 2015). The sections of SEPA DEM data that derive from lower resolution airborne SAR data may likely be less accurate than the areas covered by LiDAR (Sibona et al., 2016; Tulldahl et al., 2015, Coveney 2013a, Hodgson, M. E., & Bresnahan, 2004). However, the study area does appear to be coincident (SEPA, 2015) with the higher quality 5-metre DEM data deriving from airborne LiDAR (SEPA, 2015). As noted previously, airborne LiDAR is widely regarded as the most suitable source of commercial DEM data for use in flood modelling applications (Croke et al., 2013; Turner et al,. 2013; Poulter & Halpin, 2008). Therefore, the SEPA risk maps provided the best possible basis for assessing and demonstrating the potential for using UAV DEM data in this instance. The SEPA flood depth data were also subsequently used to assess the relative potential of each UAV DEM in modelling a single flood event.

Inter-comparison of flood predictions

Flood records from the Scottish Environmental Protection Agency (SEPA) river flood gauge at Killermont (Figure 8) indicated that the largest recorded flood event on this section of the River Kelvin was 3.781m above zero datum (SEPA, 2016). The purpose of this study is to assess the potential of UAV DEM data for local flood risk modelling, not to present what might be misinterpreted as a map of any actual flood event. Therefore, a slightly smaller magnitude theoretical flood event of 3m was used to evaluate the relative performance of each of the DEMs in predicting flood extents (Figure 8).

The zero GCP DEM performed exceptionally poorly (Figure 8), suggesting that a 3m flood event would essentially have no spatial impact. Comparing this with the flood prediction that was based upon the 61 GCP DEM (the DEM for which there was most certainty as to its accuracy) revealed a tiny 2.3% spatial overlap (Table 4) indicating that the zero GCP DEM was wholly unsuitable for use in flood prediction. The 5 GCP DEM performed poorly also, delineating a flood risk zone that was less than 45% of the flood risk area

predicted by the best performing DEM (Table 4). The 10 GCP DEM achieved a better result, though this predicted a flood risk zone of that was approximately 15% smaller than best DEM.

Spatial predictions of flood risk were more or less identical after a minimum of 15 GCP DEM was used. Similar to what was observed in the DEM accuracy evaluation, the 15 GCP DEM performed more or less identically to the 30GCP, 45 GCP and 61 GCP DEMs. Almost identical flood risk zones were predicted using the 15, 30, 45 and 61 GCP DEMs; all of these being as little as 1 or 2% different in terms of spatial overlap (Table 4). These similarities supported the conclusion that 15, 30, 45 and 61 GCP DEMs all produced useable spatial predictions of actual flood risk.

Figure 8: Flood models for a 3-metre flood event, using DEMs generated from differing numbers of ground control points.

Flood gauge location

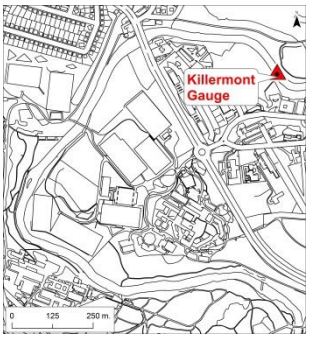

Flood model – 0 GCP DEM

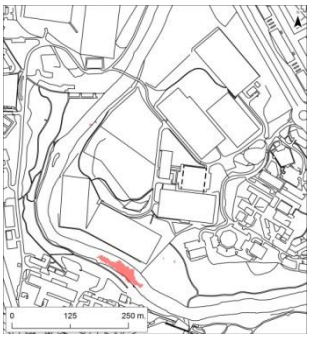

Flood model – 5 GCP DEM

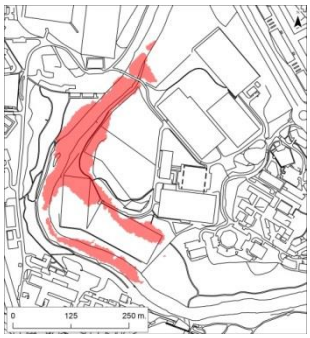

Flood model – 10 GCP DEM

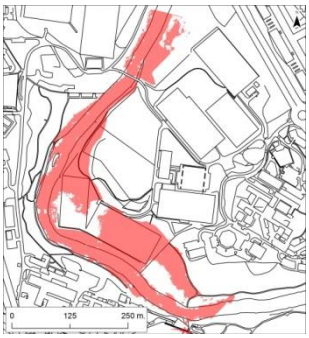

Flood model – 15 GCP DEM

Flood model – 30 GCP DEM

Flood model – 45 GCP DEM

Flood model – 61 GCP DEM

Table 4: Flood model performance.

flood model	x (m)	y (m)	cell m2	predict flood (m2)	% area of best DEM prediction	% positive overlap area	% negative overlap area
0gcpflood	2.68	2.68	7.167	1777	2.3	1	0
5gcpflood	2.63	2.63	6.938	33788	44.5	90.7	9.3
10gcpflood	0.14	0.14	0.020	65829	86.6	97.1	2.9
15gcpflood	0.14	0.14	0.020	76302	100.4	98.3	1.7
30gcpflood	0.14	0.14	0.020	76379	100.5	98.6	1.4
45gcpflood	0.14	0.14	0.020	75996	100.0	99.0	1.0
61gcpflood	0.14	0.14	0.020	75977	100	100	0

4. Discussion

4.1 Data accuracy using no GCPs

The orthoimage generated without ground reference data was characterised by positioning errors of up to 6m, and mean errors of just under 3m. Errors were generally smaller in portions of the survey area that were at similar elevations to the launch point, but were approximately twice as large elsewhere. While offering potential in terms of providing high-resolution on-demand imagery, more accurate (though admittedly lower resolution, and not on-demand) georeferenced image data may often be available from free online sources, or from established aerial image mapping data providers.

The DEM that was generated from internal positioning and orientation data (i.e. the zero GCP DEM) was characterised by elevation errors that ranged up to 6m, with 95% of these errors as large as 5m, and with an overall RMS elevation error of 2.2m. This DEM also failed to represent all but the most prominent 3D features (a few buildings were vaguely discernible in the data) presenting an unrealistically smooth model of the topography. It should be noted that the simple GPS and IMU sensors that are used in many lightweight UAVs are not generally expected to produce useable DEM data in the absence of external GNSS reference data. However, this may not always be obvious to all of the potential users who may consider using lightweight UAVs in environmental modelling applications.

4.2 Data accuracy using a small number of GCPs

Using as a little as 5 GCPs for orthoimage generation produced significantly improved results. Mean horizontal orthoimage errors reported by PhotoScan reduced to 0.28m, suggesting that even a relatively small number of external GNSS GCPs (one for every 6 hectares when 5 GCPs were used) may produce a useable orthoimage. Doubling the number of GCPs to 10 produced additional marked improvements, with mean horizontal errors reducing to 0.14m.

DEM Elevation errors were quantified in ArcGIS only, because it provided a range of accuracy statistics than were unavailable in the photogrammetric processing software. The 5 GCP DEM was characterised by a maximum to minimum range of elevation errors of approximately 5m, 95% of these being just a little under 4m, and the overall RMS elevation error was 1.3m. The 10 GCP DEM performed better, with a maximum to minimum range of just under 1.5m, 95% of these being just a little under 1.4m, and the overall RMS error for elevation of 0.34m. However, many potential DEM users might consider these errors to be a bit too large to be used in environmental modelling, especially for flood modelling, where elevation accuracy is of critical importance.

4.3 Optimal balance of data accuracy and number of GCPs

Orthoimage and DEM accuracy improved very substantially when 15 GCPs were used. Orthoimage positioning errors in this case (the very slightly larger errors that were reported externally in ArcGIS are outlined here) reduced to a total range of under 0.4m, with 95% of these positioning errors at ≤0.11m and with an overall RMS horizontal error of 0.08m. DEM elevation accuracies improved markedly also when 15 GCPs were utilised for photogrammetric processing, with a total error range of 0.5m, 95% of elevation errors ≤0.20m, and an overall RMSE elevation error of just 0.08m. These results confirm the best results that are reported in other studies (Tamminga et al., 2015; Uysal et al., 2015), which evaluate the potential DEM accuracies of similar lightweight UAV systems in conjunction with GNSS ground reference data.

4.4 Data accuracy using larger numbers of GCPs

Orthoimages generated using 30, 45 and 61 GCPs were characterised by very similar accuracies to when 15 GCPs were used. Maximum horizontal errors remained the same, and mean x and mean y errors reduced

very slightly (PhotoScan statistics reported maximum and mean horizontal errors only). The 95% positioning errors in the 61 GCP orthoimage were identical to the 15 GCPs orthoimage, and marginally smaller RMS positioning errors (as reported in ArcGIS 10.2) were observed compared to the 15 GCP orthoimage.

DEMs derived from the use of 30, 45 GCPs were characterised by almost identical elevation errors as when 15 GCPs were used also, with very slightly smaller 95% elevation errors to ≤0.19 m, and an identical RMSE of 0.08m being achieved in these cases. No further increases in elevation accuracy were observed in the 61 GCP DEM, where 95% of elevation errors were ≤0.21m and RMS elevation errors were 0.09m.

It is important to note that these DEM accuracies are very comparable to what can be expected from medium resolution (1 to 2m horizontal sampling) airborne LiDAR (Sibona et al., 2016; Croke et al., 2013; Coveney, 2013a; Schmid et al., 2011; Hodgson & Bresnahan, 2004), although UAV derived DEMs will typically cover a very much smaller area than airborne LiDAR data. Nevertheless, the accuracies that were achieved do clearly demonstrate the potential to generate useful DEMs from a relatively simple lightweight UAV with external GNSS ground reference data.

4.5 Flood modelling results

No published or unpublished data could be found that tied geographic flood limits of any single flood event to contemporaneous measured flood depths, and the SEPA flood risk categories refer to nominal rather than numeric levels of flood risk. However, it was possible to use local SEPA river-gauge flood depth data to infer the flood depths that corresponded to each SEPA flood risk zone. These flood depths were then used to model the same flood risk zones with the UAV DEM data. Very similar flood risk zones were observed within the SEPA flood risk mapping and the UAV DEM flood prediction mapping. While it should be noted that the SEPA risk mapping is itself a model output (derived from airborne LiDAR at 5-metre ground sampling intervals) the close similarities observed do demonstrable the potential of UAV DEMs to provide the accuracies required for useful river flood prediction modelling.

It was also possible however to conduct a cross-comparison of the performance of UAV DEM flood risk models when they were applied to a single theoretical flood event. The results closely mirrored the outcomes of the empirical DEM accuracy tests, with the most consistent results being achieved with those DEMs that were generated using more than a certain minimum number of GCPs.

The zero GCP DEM proved to be useless, outlining a flood risk zone that was 2.5% the size of the at risk area that the best DEMs predicted flood impacts for. The 5 GCP and 10 GCP DEM performed better, but unsatisfactorily. Excellent flood prediction results were achieved using the 15 GCP DEM, which represented the use of approximately one GCP for every 2 hectares of ground area. Flood predictions that used the 30 GCP DEM, 45 GCP DEM and 61 GCP DEM achieved no discernible improvements over the 15 GCP DEM, suggesting that the best 4 DEMs all delineated flood risk equally effectively.

5. Summarised Conclusions

- Orthoimagery generated using internal positioning and orientation was not accurate enough to be used as a large-scale mapping product
- The DEM that was created using internal positioning and orientation sensors was characterised by elevation errors that were too large to be used in any environmental modelling application
- Good orthoimage accuracies were achieved using as few as one ground control point for every 6 hectares of ground area
- Exceptionally accurate orthoimages and DEMs were generated when using approximately one GCP for every 2 hectares of ground area
- Doubling and re-doubling the number of GCPs produced no better results
- Flood risk maps from the UAV DEM were very similar to published risk maps, demonstrating the potential of UAV DEM data for local-scale flood prediction
- Strikingly similar flood risk predictions derived from DEMs generated using larger numbers of GCPs suggested that the best four DEMs all produced reliable flood prediction results.

References

Agisoft. 2014). “Agisoft PhotoScan User Manual: Professional Edition, Version 1.1.” Agisoft Ltd. St. Petersburg, Russia.

Agisoft. 2016. Agisoft User Forum. Accessed online at http://www.agisoft.com/forum/index.php?topic=89.0 July 2016.

Anderson, K., & Gaston, K. J. 2013. “Lightweight unmanned aerial vehicles will revolutionize spatial ecology.” Frontiers in Ecology and the Environment, 11(3), 138-146.

Bates, P. D., & De Roo, A. P. J. 2000. “A simple raster-based model for flood inundation simulation.” Journal of Hydrology, 236(1), 54-77.

Bürkle, A., Segor, F., & Kollmann, M. 2011. “Towards autonomous micro UAV swarms.” Journal of Intelligent & Robotic Systems, 61(1-4), 339-353.

CAA. 2016. United Kingdom Civil Aviation Authority Guidelines on the operation of unmanned aerial vehicles. http://www.caa.co.uk/unmannedaircraft/ Accessed online, July, 2016.

Cobby, D. M., Mason, D. C., & Davenport, I. J. 2001. “Image processing of airborne scanning laser altimetry data for improved river flood modelling.” ISPRS Journal of Photogrammetry and Remote Sensing, 56(2), 121-138.

Coveney, S. 2013a. “Association of elevation error with surface type, vegetation class and data origin in discrete-returns airborne LiDAR.” International Journal of Geographical Information Science, 27(3), 467-483.

Coveney, S. 2013b. 2013. “Land Cover Dependent Error in Intermap IFSAR DTM.” Photogrammetric Engineering & Remote Sensing. 79 (3), 277-286.

Coveney, S., & Fotheringham, A. S. 2011a. “The impact of DEM data source on prediction of flooding and erosion risk due to sea-level rise.” International Journal of Geographical Information Science, 25(7), 1191-1211.

Coveney, S., & Stewart Fotheringham, A. 2011b. “Terrestrial laser scan error in the presence of dense ground vegetation.” The Photogrammetric Record, 26(135), 307-324.

Coveney, S., Fotheringham, A. S., Charlton, M., & McCarthy, T. 2010. “Dual-scale validation of a medium-resolution coastal DEM with terrestrial LiDAR DSM and GPS.” Computers & Geosciences, 36(4), 489-499.

Croke, J., Todd, P., Thompson, C., Watson, F., Denham, R. and Khanal, G., 2013. The use of multi temporal LiDAR to assess basin-scale erosion and deposition following the catastrophic January 2011 Lockyer flood, SE Queensland, Australia. Geomorphology, 184, pp.111-126.

Darwin, N., Ahmad, A., & Zainon, O. 2014. The potential of unmanned aerial vehicle for large scale mapping of coastal area.” In IOP Conference Series: Earth and Environmental Science (Vol. 18, No. 1, p. 012031). IOP Publishing.

García-Pintado, J., Neal, J. C., Mason, D. C., Dance, S. L., & Bates, P. D. 2013. “Scheduling satellite-based SAR acquisition for sequential assimilation of water level observations into flood modelling.” Journal of Hydrology, 495, 252-266.

Haile, A. T., & Rientjes, T. H. M. 2005. “Effects of LiDAR DEM resolution in flood modelling: a model sensitivity study for the city of Tegucigalpa, Honduras.” ISPRS WG III/3, III/4, 3, 12-14.

Heritage, G., & Large, A. 2009. Laser scanning for the environmental sciences. John Wiley & Sons.

Hodgson, M. E., & Bresnahan, P. 2004. “Accuracy of airborne LiDAR-derived elevation.” Photogrammetric Engineering & Remote Sensing, 70(3), 331-339

Holmes, K. W., Chadwick, O. A., & Kyriakidis, P. C. 2000. “Error in a USGS 30-meter digital elevation model and its impact on terrain modelling.” Journal of Hydrology, 233(1), 154-173.

Horritt, M. S., & Bates, P. D. 2002. “Evaluation of 1D and 2D numerical models for predicting river flood inundation.” Journal of Hydrology, 268(1), 87-99.

Jarvis, A., Reuter, H. I., Nelson, A., & Guevara, E. 2008. Hole-filled SRTM for the globe Version 4. Available from the CGIAR-CSI SRTM 90m Database (http://srtm. csi. cgiar. org).

Klemas, V. V. 2015. “Coastal and environmental remote sensing from unmanned aerial vehicles: An overview.” Journal of Coastal Research, 31(5), 1260-1267.

Kulkarni, A. T., Mohanty, J., Eldho, T. I., Rao, E. P., & Mohan, B. K. 2014. “A web GIS based integrated flood assessment modelling tool for coastal urban watersheds.” Computers & Geosciences, 64, 7-14.

Küng, O., Strecha, C., Beyeler, A., Zufferey, J. C., Floreano, D., Fua, P., & Gervaix, F. 2011. The accuracy of automatic photogrammetric techniques on ultra-light UAV imagery. In UAV-g 2011-Unmanned Aerial Vehicle in Geomatics (No. EPFL-CONF-168806).

Poulter, B., & Halpin, P. N. 2008. “Raster modelling of coastal flooding from sea-level rise.” International Journal of Geographical Information Science, 22(2), 167-182.

Remondino, F., Barazzetti, L., Nex, F., Scaioni, M., & Sarazzi, D. 2011. “UAV photogrammetry for mapping and 3d modelling–current status and future perspectives.” International Archives of the Photogrammetry, Remote Sensing and Spatial Information Sciences, 38(1), C22.

Sanders, B. F. 2007. “Evaluation of on-line DEMs for flood inundation modelling.” Advances in Water Resources, 30(8), 1831-1843.

Schmid, K. A., Hadley, B. C., & Wijekoon, N. 2011. “Vertical accuracy and use of topographic LIDAR data in coastal marshes.” Journal of Coastal Research, 27(6A), 116-132.

SenseFly. 2011. Swinglet Cam User Manual. Revision 2.2. SenseFly. Cheseaux-sur-Lausanne, Switzerland.

SEPA, 2016a. Scottish Environmental Protection Agency flood gauge records. Killermont flood gauge records accessed online at http://apps.sepa.org.uk/waterlevels/default.aspx?sd=t&lc=133099 July 2016.

SEPA, 2016b. Scottish Environmental Protection Agency Flood risk online mapping system, accessed online at http://map.sepa.org.uk/floodmap/map.htm December, 2016.

SEPA, 2015, River flooding summary: Methodology and mapping, accessed online at https://www.sepa.org.uk/media/163406/river_flooding_summary.pdf December 2016.

Şerban, G., Rus, I., Vele, D., Breţcan, P., Alexe, M., & Petrea, D. 2016. “Flood-prone area delimitation using UAV technology, in the areas hard-to-reach for classic aircrafts: case study in the north-east of Apuseni Mountains, Transylvania.” Natural Hazards, 1-16.

Sibona, E., Vitali, A., Meloni, F., Caffo, L., Dotta, A., Lingua, E., Motta, R. and Garbarino, M., 2016. Direct Measurement of Tree Height Provides Different Results on the Assessment of LiDAR Accuracy. Forests, 8(1), p.7.

SmartNet. 2016. SmartNet: Network RTK. Accessed online at http://uk.smartnet-eu.com/network-rtk_146.htm July 2016

Sona, G., Pinto, L., Pagliari, D., Passoni, D., & Gini, R. 2014. “Experimental analysis of different software packages for orientation and digital surface modelling from UAV images.” Earth Science Informatics, 7(2), 97-107.

Tamminga, A., Hugenholtz, C., Eaton, B., & Lapointe, M. 2015. “Hyperspatial remote sensing of channel reach morphology and hydraulic fish habitat using an unmanned aerial vehicle (UAV): a first assessment in the context of river research and management.” River Research and Applications, 31(3), 379-391.

Tulldahl, H.M., Bissmarck, F., Larsson, H., Grönwall, C. and Tolt, G., 2015, October. Accuracy evaluation of 3D LiDAR data from small UAV. In SPIE Security+ Defence (pp. 964903-964903). International Society for Optics and Photonics.

Turner, A.B., Colby, J.D., Csontos, R.M. and Batten, M., 2013. Flood modelling using a synthesis of multi-platform LiDAR data. Water, 5(4), pp.1533-1560.

Udin, W. S., & Ahmad, A. 2014. “Assessment of photogrammetric mapping accuracy based on variation flying altitude using unmanned aerial vehicle.” In IOP Conference Series: Earth and Environmental Science (Vol. 18, No. 1, p. 012027). IOP Publishing.

Unger, J., Reich, M., & Heipke, C. 2014, “UAV-based photogrammetry: monitoring of a building zone.” The International Archives of Photogrammetry, Remote Sensing and Spatial Information Sciences, 40(5), 601.

Uysal, M., Toprak, A. S., & Polat, N. 2015. “DEM generation with UAV Photogrammetry and accuracy analysis in Sahitler hill.” Measurement, 73, 539-543.

Vallet, J., Panissod, F., Strecha, C., & Tracol, M. 2011. “Photogrammetric performance of an ultralight weight Swinglet UAV.” In UAV-g (No. EPFL-CONF-169252).

Verstraeten, G. 2006. “Regional scale modelling of hillslope sediment delivery with SRTM elevation data.” Geomorphology, 81(1), 128-140.